Long wavelength gradient drift instability in Hall plasma devices. II. Applications

Winston Frias, Andrei I. Smolyakov, Igor D. Kaganovich, and Yevgeny Raitses

Citation: Physics of Plasmas (1994-present) **20**, 052108 (2013); doi: 10.1063/1.4804281
View online: http://dx.doi.org/10.1063/1.4804281
View Table of Contents: http://scitation.aip.org/content/aip/journal/pop/20/5?ver=pdfcov
Published by the AIP Publishing

Long wavelength gradient drift instability in Hall plasma devices. II. Applications

Winston Frias,[1,a)] Andrei I. Smolyakov,[1] Igor D. Kaganovich,[2] and Yevgeny Raitses[2]
[1]*Department of Physics and Engineering Physics, University of Saskatchewan, 116 Science Place, Saskatoon SK S7N 5E2, Canada*
[2]*Princeton Plasma Physics Laboratory, Princeton, New Jersey 08543, USA*

(Received 24 January 2013; accepted 22 April 2013; published online 8 May 2013)

Hall plasma devices with electron $E \times B$ drift are subject to a class of long wavelength instabilities driven by the electron current, gradients of plasma density, temperature, and magnetic field. In the first companion paper [Frias *et al.*, Phys. Plasmas **19**, 072112 (2012)], the theory of these modes was revisited. In this paper, we apply analytical theory to show that modern Hall thrusters exhibit azimuthal and axial oscillations in the frequency spectrum from tens KHz to few MHz, often observed in experiments. The azimuthal phase velocity of these modes is typically one order of magnitude lower than the $E \times B$ drift velocity. The growth rate of these modes scales inversely with the square root of the ion mass, $\sim 1/\sqrt{m_i}$. It is shown that several different thruster configurations share the same common feature: the gradient drift instabilities are localized in two separate regions, near the anode and in the plume region, and absent in the acceleration region. Our analytical results show complex interaction of plasma and magnetic field gradients and the $E \times B$ drift flow as the sources of the instability. The special role of plasma density gradient is revealed and it is shown that the previous theory is not applicable in the region where the ion flux density is not uniform. This is particularly important for near anode region due to ionization and in the plume region due to diverging ion flux. © *2013 AIP Publishing LLC*.
[http://dx.doi.org/10.1063/1.4804281]

I. INTRODUCTION

Hall plasmas devices with $\mathbf{E} \times \mathbf{B}$ electron drift demonstrate wide range of turbulent fluctuations. These fluctuations are probably the reason for the observed anomaly in the electron transport across the magnetic field[1–3] and other nonlinear phenomena such as coherent rotating structures (spoke).[4,5] Understanding of the mechanisms of the coherent structures and anomalous transport requires the detailed study of linear instabilities in Hall plasma devices. In Ref. 6 (Part I), we have revisited the earlier derivations of the instability due to density and magnetic field gradients[7,8] and shown that the effects of plasma compressibility were not fully included in previous theory and quantitative corrections are required for accurate description of the growth rate and real part of frequency. We have also extended the fluid model to include the dynamics of electron temperature and developed a three-field fluid model that includes the electron energy equation providing a more accurate model of the electron response.

The main goal of this work is to apply the analytical results obtained in Ref. 6 to realistic configurations of Hall thrusters. We also discuss here how the previous models[9–12] for gradient drift type modes are related to the advanced model put forward in Ref. 6. We investigate how plasma parameters, e.g., the equilibrium $\mathbf{E} \times \mathbf{B}$ drift, gradients of plasma density, temperature, and magnetic field, affect the characteristics, excitation conditions, and localization of the linear instabilities and discuss how these may be related to some experimentally observed features, such as spoke generation. We have used the experimental data for a 2 kW Hall thruster from the Hall Thruster experiment (HTX) at Princeton Plasma Physics Laboratory (PPPL),[13,14] numerically simulated profiles for the plasma density, potential, electron temperature, and magnetic field obtained using the numerical code HPHall-2 for the SPT-100 thruster[15] as well as the data from the coaxial magnetoisolated longitudinal anode (CAMILA) Hall thruster at the Technion-Israel Institute of Technology.[16] Our analytical results show complex interaction of plasma and magnetic field gradients in destabilization of the $\mathbf{E} \times \mathbf{B}$ drift flow. In earlier theory,[7] the density gradient was absent as an independent parameter controlling the instability because the authors of Ref. 7 assumed the absence of ionization and neglected the ion flux divergence. Experimental data show that these assumptions are not valid, and, as a result, the theory of Ref. 7 is inapplicable in such regions. Our theory retains the plasma density gradient as an independent parameter, which is critically important for valid predictions of the stability of Hall thrusters.

This paper is organized as follows. In Sec. II, a summary of the findings in Ref. 6 and review of previous work will be provided. In Sec. III, the two and three field model dispersion relations will be solved for thrusters under study. In Sec. IV, the conclusions of this paper will be presented.

II. GRADIENT DRIFT INSTABILITIES

Complete analysis of the gradient drift instability is presented in Part I.[6] Here, we give a summary to facilitate the

[a)]Electronic mail: wpf274@mail.usask.ca

comparison of different models. The analysis of linear instability is done for the simplified geometry of a coaxial Hall thruster with the equilibrium electric field $\mathbf{E}_0 = E_0\hat{\mathbf{x}}$ in the axial direction, and with inhomogeneous density $n = n_0(x)$ and electron temperature $T = T_e(x)$. Locally, Cartesian coordinates (x, y, z) are introduced with the z coordinate in the radial direction and y in the symmetrical azimuthal direction. The magnetic field is assumed to be predominantly in the radial direction, $\mathbf{B} = B_0(x)\hat{\mathbf{z}}$. In the two field model, assuming constant electron temperature, the ion and electron densities are given by the expressions[6]

$$\frac{\tilde{n}_i}{n_0} = \frac{k_\perp^2 c_s^2}{(\omega - k_x v_0)^2}\frac{e\phi}{T_e}, \tag{1}$$

$$\frac{\tilde{n}_e}{n_0} = \frac{\omega_* - \omega_D}{\omega - \omega_0 - \omega_D}\frac{e\phi}{T_e}, \tag{2}$$

where $\omega_0 = k_y u_0$, $u_0 = -\hat{\mathbf{y}}cE_{0x}/B_0$ is the electric drift velocity in azimuthal $\hat{\mathbf{y}}$ direction, v_0 is the ion drift velocity in the axial $\hat{\mathbf{x}}$ direction, $\omega_D = -2k_y cT_e/(eB_0L_B)$ and $\omega_* = -k_y cT_e/(eB_0L_N)$ are the magnetic and density gradient drift frequencies, $1/L_B = \partial \ln B_0/\partial x$ and $1/L_N = \partial \ln n_0/\partial x$ are the magnetic field and density characteristic variation lengths.

Using the quasineutrality condition, the last two equations lead to the following dispersion equation:[6]

$$\frac{\omega_* - \omega_D}{\omega - \omega_0 - \omega_D} = \frac{k_\perp^2 c_s^2}{(\omega - k_x v_{0i})^2}, \tag{3}$$

with explicit solution in the form

$$\omega - k_x v_0 = \frac{1}{2}\frac{k_\perp^2 c_s^2}{\omega_* - \omega_D} \pm \frac{1}{2}\frac{k_\perp^2 c_s^2}{\omega_* - \omega_D} \times \sqrt{1 + 4\frac{k_x v_0}{k_\perp^2 c_s^2}(\omega_* - \omega_D) - 4\frac{k_y^2}{k_\perp^2}\rho_s^2\Delta}, \tag{4}$$

where $\Delta = (\partial \ln B_0^2/\partial x + eE_0/T_e)(\partial \ln(n_0/B_0^2)/\partial x)$, $\rho_s^2 = T_e m_i c^2/e^2 B_0^2$.

From Eq. (4), the conditions for instability in the two field model, assuming purely azimuthal propagation can be written as

$$\left(\frac{\partial}{\partial x}\ln B_0^2 + \frac{eE_0}{T_e}\right)\frac{\partial}{\partial x}\ln\left(\frac{n_0}{B_0^2}\right) > \frac{1}{4\rho_s^2}. \tag{5}$$

When fluctuations of the electron temperature are included, the electron continuity and momentum equations are complemented by the electron energy balance equation resulting in a three-field model: n, T_e, and ϕ. The following cubic dispersion relation was obtained:[6]

$$\frac{-(\omega - \omega_0)(\omega_D - \omega_*) + \omega_D\left(\omega_{*T} - \frac{7}{3}\omega_*\right) + \frac{5}{3}\omega_D^2}{(\omega - \omega_0)^2 - \frac{10}{3}\omega_D(\omega - \omega_0) + \frac{5}{3}\omega_D^2} = \frac{k_y^2 c_s^2}{\omega^2}, \tag{6}$$

where $\omega_{*T} = -k_y cT_{e0}/eB_0L_T$ and $1/L_T = \partial \ln T_{e0}/\partial x$.

The dispersion relation in Eq. (6), can be written as

$$a\omega^3 + b\omega^2 + c\omega + d = 0, \tag{7}$$

where

$$a = \omega_* - \omega_D,$$
$$b = -k_y^2 c_s^2 - \omega_*\omega_0 - \frac{7}{3}\omega_*\omega_D + \omega_0\omega_D + \frac{5}{3}\omega_D^2 + \omega_{*T}\omega_D,$$
$$c = 2k_y^2 c_s^2\omega_0 + \frac{10}{3}k_y^2 c_s^2\omega_D,$$
$$d = -k_y^2 c_s^2\omega_0^2 - \frac{10}{3}k_y^2 c_s^2\omega_0\omega_D - \frac{5}{3}k_y^2 c_s^2\omega_D^2.$$

It is well known that Eq. (7) will have complex roots (one real and two complex conjugates) if the following condition is met:

$$\Delta = 18abcd - 4b^3 d + b^2 c^2 - 4ac^3 - 27a^2 d^2 < 0. \tag{8}$$

As can be seen from Eq. (8), the three field model instability conditions cannot be easily expressed in a succint way, similar to the one expressed in Eq. (5).

The long wavelength instabilities described by Eqs. (4) and (6) have the equilibrium electron flow as the main driving source of the instability, which is triggered by the presence of the gradients of plasma density, temperature, and magnetic field. The Hall plasma with equilibrium electron current can be destabilized by the density gradient alone: the corresponding instability became known as Simon-Hoh instability.[9,10,17] In purely collisionless case, it was called the anti-drift instability,[11] because of the inverse dependence of the real part of the frequency on the drift frequency. The dispersion relation for anti-drift mode follows from Eq. (4) assuming no magnetic field gradients:

$$\frac{\omega_*}{\omega - \omega_0} = \frac{k_\perp^2 c_s^2}{(\omega - k_x v_{0i})^2}. \tag{9}$$

The condition $\mathbf{E}_0 \cdot \nabla n_0 > 0$ was noted as required for the Simon-Hoh instability.[12] A more accurate condition follows from Eq. (4), $(eE_0/T_e)(\partial/\partial x)\ln(n_0) > 1/(4\rho_s^2)$.

Sakawa *et al.*[12] have considered the so called modified Simon-Hoh instability by including the finite equilibrium ion velocity (in azimuthal direction) that may occur due to partial magnetization of ion motion. The amplitude of this drift velocity for ions with large Larmor radius was estimated for Maxwellian plasma by averaging the $\mathbf{E} \times \mathbf{B}$ drift over the ion gyroradius[12]

$$v_{\theta i} = c\frac{E_0}{B_0}e^{-b}I_0(b), \tag{10}$$

where $b = k_\perp^2\rho_i^2 \gg 1$ is the parameter characterizing the large Larmor radius parameter, $k_\perp \sim L^{-1}$, L is the characteristic length scale of the electric field inhomogeneity. The resulting dispersion relation[12] then is

$$\frac{\omega_*}{\omega-\omega_0}=\frac{k_\perp^2 c_s^2}{(\omega-k_x v_{0i}-k_y v_{\theta i})^2}. \tag{11}$$

Essentially, this is the anti-drift mode equation (9) with an additional azimuthal ion velocity. The addition of the finite $v_{\theta i}$ to the ion response changes the real part of the frequency by an additional factor of $k_y v_{\theta i}$, but does not affect the growth rate of the long wavelength modes in a significant way as long as $v_{\theta i} < u_0$. The $v_{\theta i}$ velocity from Eq. (10) has a value of around 0.1%–5% of u_0 for the plasma parameters used in this paper and will be neglected for the most part of our calculations.

The authors of Refs. 7 and 18 considered the related mode in plasma with inhomogeneous magnetic field. They also included the electromagnetic effects and electron inertia which are not important for typical plasma parameters in Hall thrusters. Esipchuk and Tilinin[7] have also included the electron drift effects related to plasma density gradient. However, they have made an additional assumption that plasma density gradient can be related to the gradient of the electric potential via the density conservation equation and assuming the ballistic acceleration of ions. Thus, they have used the relations

$$n_0(x)v_{0i}(x)=const, \tag{12}$$

$$v_{0i}\frac{dv_{0i}}{dx}=-\frac{e}{m_i}E_0(x), \tag{13}$$

to find the density gradient in terms of the electron equilibrium drift velocity u_0

$$\frac{\partial \ln n_0}{\partial x}=u_0\frac{\Omega_i}{v_{0i}^2}. \tag{14}$$

They also defined the magnetic drift velocity u_B via the relation

$$u_B=\frac{v_{0i}^2}{\Omega_i}\frac{\partial \ln B_0}{\partial x}. \tag{15}$$

With these definitions, the dispersion relation derived by Esipchuk and Tilinin[7] has the form

$$\frac{\omega_{pi}^2}{(\omega-k_x v_{0i})^2}=\frac{\omega_{pi}^2(k_y u_0-k_y u_B)}{k^2 v_{0i}^2(\omega-k_y u_0)}. \tag{16}$$

The electron inertia, electromagnetic and non-quasineutrality effects have been omitted here for ease of comparison. As it was noted above, the latter effects are small for our typical parameters. The dispersion equation (16) does not contain the drift due to density gradient explicitly since it has been replaced via the relation (14).

We can, however, rewrite this equation with explicitly retained drift frequency so it takes the form

$$\frac{\omega_*-\omega_D'}{\omega-\omega_0}=\frac{k_\perp^2 c_s^2}{(\omega-k_x v_{0i})^2}. \tag{17}$$

Here, the magnetic drift frequency is defined as $\omega_D' = -k_y c T_e/(eB_0 L_B)$, compare this with our two-fluid model equation (3). The difference between ω_D' in Eq. (17) and ω_D in our two-fluid model, Eq. (3), is due to an incomplete account of the electron flow incompressibility in Ref. 18 as discussed in Part I. Morozov has also neglected the compressibility of the electron diamagnetic flow.[18] As a result, an additional ω_D is missing in the denominator of Eq. (17), compared with Eq. (3).

In Sec. IV, we will compare the predictions based on these different models.

III. STABILITY ANALYSIS

In order to study the instabilities predicted by our two and three-field models, we use realistic profiles of the magnetic field, electric field, plasma density, and electron temperature. In this section, we will solve the dispersion relation for each model using the plasma parameters obtained in three different experiments[13,14,16] and simulations.[15]

A. PPPL HTX

In Ref. 13, plasma parameters are measured for a 2 kW laboratory Hall thruster at the Princeton Plasma Physics Laboratory. The Hall thruster has a channel length of 46 mm, an outer diameter of 123 mm, and a width of 15 mm due to the addition of two boron nitride spacers added to the inner and outer channel walls of the channel. Plasma parameters inside the thruster were measured using emissive and non-emissive electrostatic probes. Plasma parameters in the thruster plume were measured using a flat electrostatic probe of 2.54 cm diameter. The detailed discussion of the experiments and measurements is available from Ref. 13. The plasma parameters used in our paper are obtained from measurements made at the midpoint between the channel walls. The plasma density, equilibrium $E\times B$ velocity, u_0, and electron temperature obtained in the experiments reported in Ref. 13 are shown in Fig. 1. There are more than 400 measurement points with distance between each point of 0.02 cm. In these experiments, measurements were done mainly outside the thruster channel, in the plume region from $x=-0.8$ cm to $x=8.0$ cm (the exit plane is at x = 0). The corresponding gradients were calculated by taking a nine-point finite difference numerical derivative (thus with a characteristic averaging length scale of 0.2 cm). The resulting values of the gradients were again averaged. The resulting profiles are shown in Fig. 2. For these profiles, the magnetic and electric field reach their peak at around x = 0 and then decay. The plasma density is monotonically decaying as well as the temperature, except for a small region close to x = 0. This results in mainly negative gradient lengths in this region as can be seen in Fig. 2. Now that we have the gradient lengths, we can solve Eqs. (4) and (6) and obtain a position dependent growth rate for the instabilities predicted by the two and three field models. The calculated growth rates are shown in Fig. 3.

As can be seen from Fig. 3, the instability predicted by the two-field model is concentrated in two narrow regions: from x = 1.22 cm to x = 1.82 cm and from x = 5.54 cm to

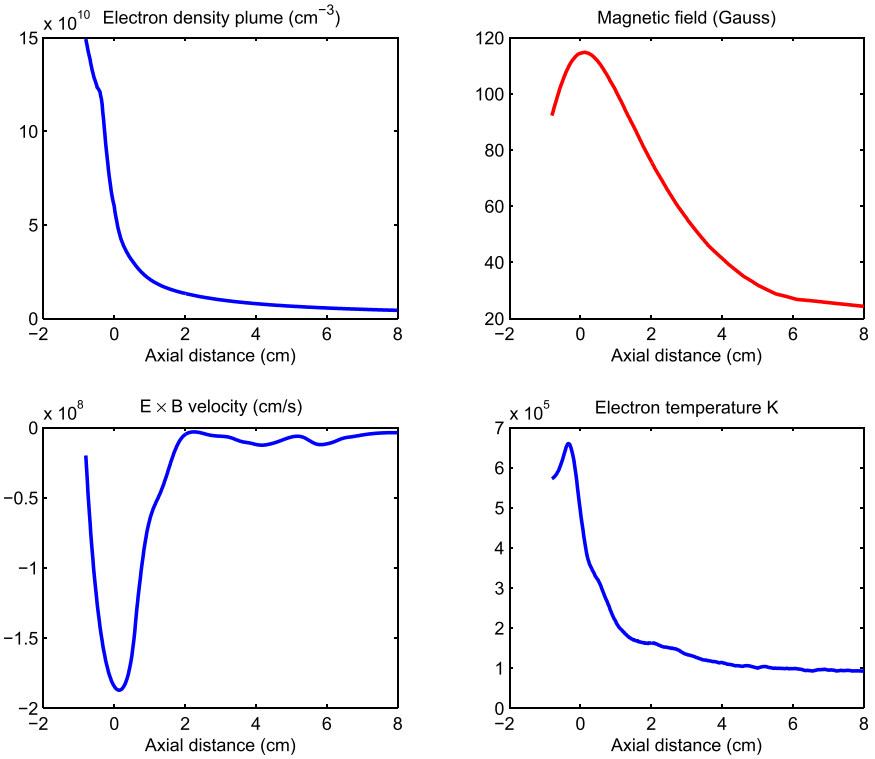

FIG. 1. Experimental profiles of the plasma density, magnetic field, electron equilibrium drift velocity, u_0, and electron temperature for the HTX thruster.[13] The exit plane is at x = 0.

x = 6.22 cm. For the instability to occur, the condition expressed above in Eq. (5) has to be met. For the profiles in Fig. 1, it is clear that in the region x < 1.22 cm, the second factor in Eq. (5), namely, $1/L_N - 2/L_B$ is negative but the first one, $eE_0/T_e + 2/L_B$ is positive, resulting in this region being stable. The region between x = 1.22 cm and x = 1.82 cm is characterized by $1/L_N - 2/L_B > 0$, and $eE_0/T_e + 2/L_B > 0$, resulting in instability. In this region, since the magnetic field is decreasing with distance, L_B is negative and the electric field satisfies the following inequality:

$$E_0 > \frac{T_e}{e}\left|\frac{2}{L_B}\right|. \tag{18}$$

This last condition suggests that in the plume region, when the magnetic field gradient length L_B is larger than twice the density gradient length L_N, the instability will occur if the

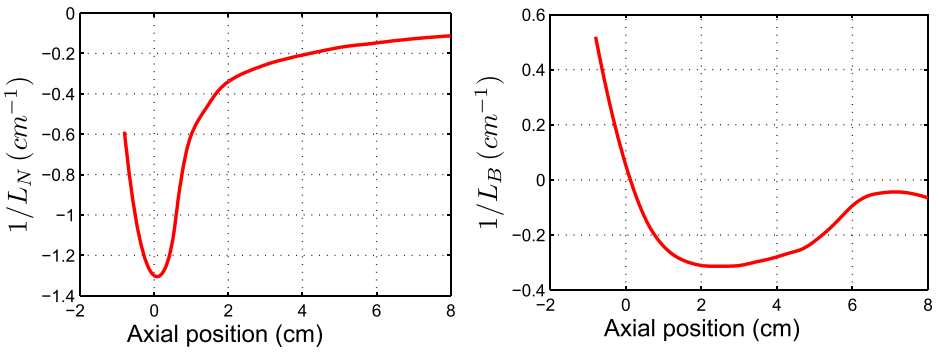

FIG. 2. Characteristic gradient lengths for the plume region of the HTX thruster.[13] The exit plane is at x = 0.

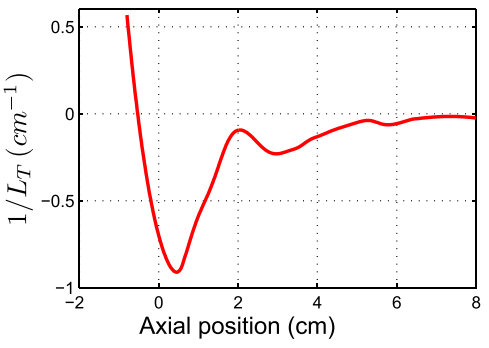

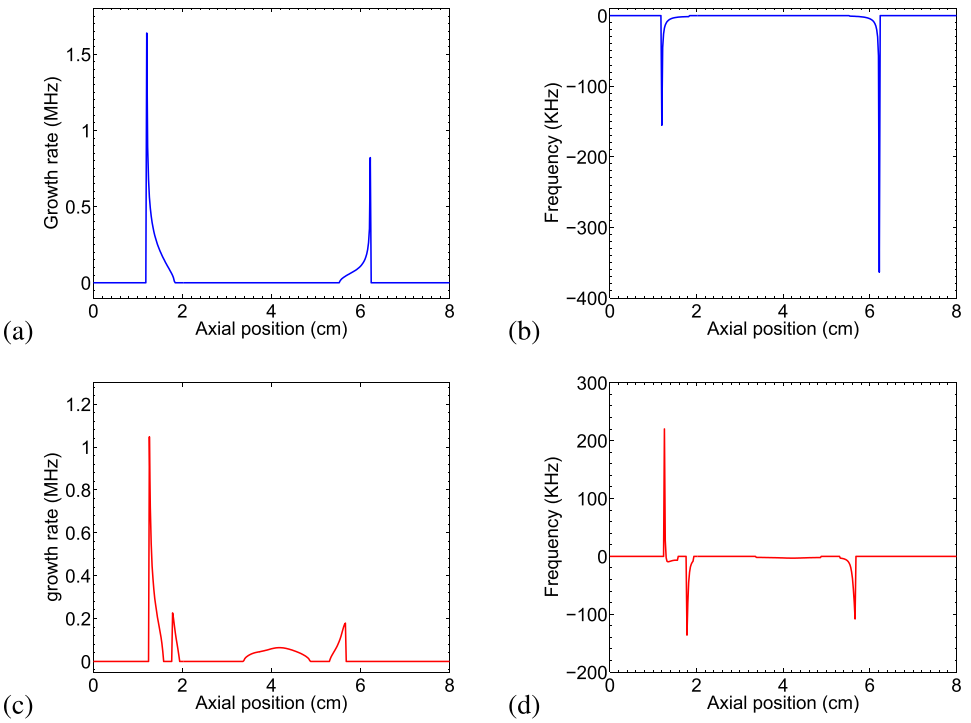

FIG. 3. Growth rate and frequency of the instabilities in the HTX thruster[13] as a function of axial distance as predicted by the two-field model ((a) and (b)) and the three-field model ((c) and (d)). The exit plane is at x = 0.

electric field is larger than a certain threshold value as expressed by Eq. (18). Also, $1/L_N - 2/L_B$ changes sign from negative to positive at x = 1.22 cm and $eE_0/T_e + 2/L_B$ changes sign from positive to negative at x = 1.82 cm. In the region between x = 1.82 cm and x = 5.54 cm, $1/L_N - 2/L_B > 0$ but the electric field is smaller than the threshold value, resulting in the instability disappearing in this region. In the region from x = 5.54 cm to x = 6.22 cm, the electric field is larger than the threshold value and the instability settles again. For x > 6.22 cm, we have $1/L_N - 2/L_B < 0$ and the instability disappears.

The real part of the frequency predicted by the two field model is negative, which is to be expected since the real part of the frequency is determined by the sign of $1/L_N - 2/L_B$. This negative frequency suggests that the azimuthal phase velocity is in the same direction as the equilibrium drift velocity u_0.

The instability predicted by the three field model is concentrated in four regions, from x = 1.26 cm to 1.56 cm, from x = 1.76 cm to x = 1.94 cm, from x = 3.34 cm to x = 4.88 cm, and from x = 5.30 cm to 5.68 cm. The maximum growth rate is smaller compared to the growth rate from the two field model. Also, apart from the region from x = 3.34 cm to x = 4.88 cm, the unstable region is narrower compared with the unstable region from the two field model. In the central unstable region, the instability is driven by an unfavorable combination of the different gradient drift velocities. The real part of the frequency is mainly negative except in the region from x = 1.26 cm to x = 1.30 cm. For typical parameters, the stability conditions are very sensitive to the temperature gradient (within the three-field model). In the region from x = 1.26 cm to x = 1.30 cm, the product of the temperature and magnetic field gradients, the factor $\omega_D\omega_{*T}$, reaches its maximum value over all other unstable regions (around 3×10^{12} Hz^2), which result in the mode destabilization and change in the rotation direction. However, this feature in the temperature gradient profile, seen Fig. 2, is difficult to confirm within the experimental measurements error.

The measurements in the HTX thruster reveal the existence of a special feature in the measured floating potential, which is below the plasma potential (for Xe, 5.77 T_e),[14] and shown in Fig. 4. The well of the floating potential is located in the region where the growth rate of the instabilities is strongest. This well in the floating potential is related to electron injection and this suggests that there may be a connection between the excitation of the instabilities in the plume region and efficiency of the electron injection in the thruster, which at the same time determines the general discharge characteristics of the device.

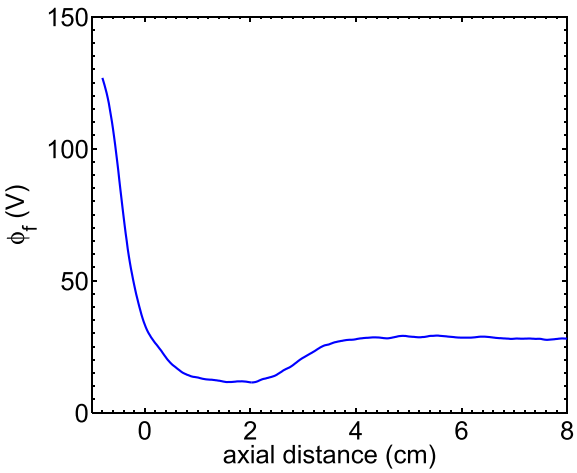

FIG. 4. Floating plasma potential for the HTX thruster.[13] The well of the plasma potential coincides with the regions where the gradient drift instabilities are strongest. The exit plane is at x = 0.

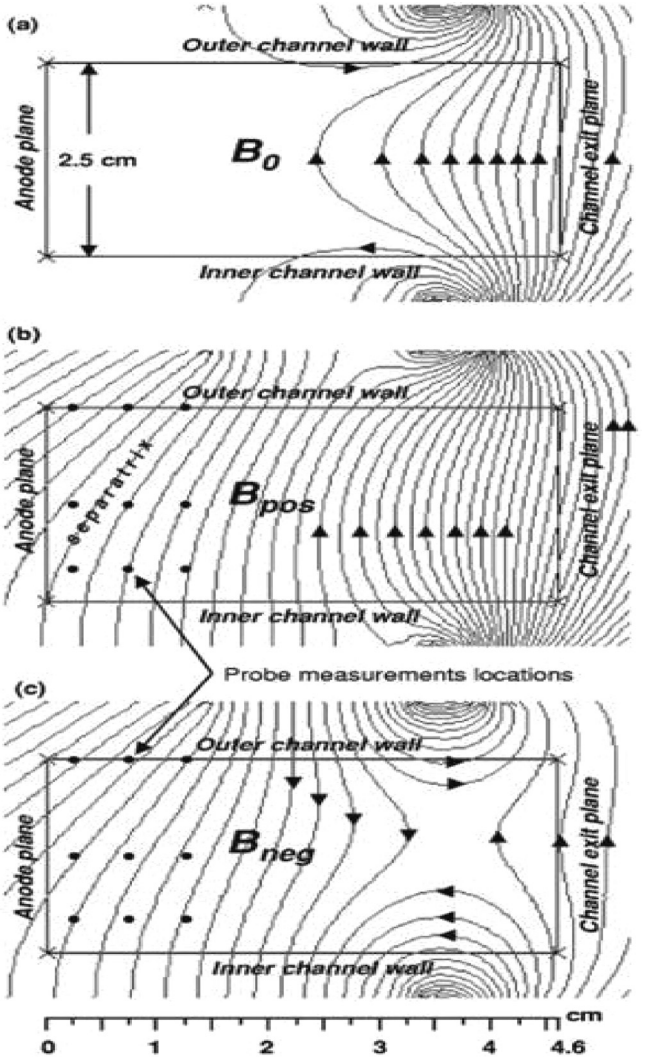

FIG. 5. Magnetic field lines in the 12.3 cm Hall thruster for three magnetic field configurations: B_0, B_{pos}, and B_{neg}. All diagrams are drawn to scale. Reprinted with permission from Phys. Plasmas **13**, 057104 (2006). Copyright 2006 American Institute of Physics.[14]

B. Near-anode region HTX thruster

There are limited measurements of plasma parameters in the near-anode region of a 12.3 cm, 2 kW Hall thruster. In Ref. 14, measurements of plasma parameters in the near-anode region are presented. In these experiments, three different configurations of the magnetic field were used to study the influence of the magnetic field profile on the anode fall in a Hall thruster. The magnetic field in the thruster is created by one inner and two outer electromagnetic coils. The currents in the inner and in one of the outer coils are kept constant while the current supplied to the another outer coil, which is placed near the anode, is changed in order to produce three different configurations of the magnetic field, B_0, B_{pos}, and B_{neg},[14] as shown in Fig. 6. The magnetic field configuration B_0 has negligible magnetic field in the near anode region, the magnetic field for configuration B_{pos} is between 60 and 80 G in the near anode region and between −60 and −80 G for the B_{neg} configuration. In the B_{pos} and B_{neg} configurations, the magnetic field in the near anode region is comparable to the magnetic field in the acceleration region. The cusp configuration of the magnetic field B_{neg} is similar to the magnetic field in other devices such as the Cylindrical Hall Thruster (CHT).[14] The magnetic field lines for the three configurations can be seen in Fig. 5. Plasma measurements were performed in three different axial positions, at 2 mm, 7 mm, and 12 mm from the anode and at three different radial positions, at the outer wall, R = 62 mm, at the midpoint of the channel, R = 49 mm and near the inner wall, R = 41 mm. The measured electron temperature and plasma density at the midpoint of the channel are shown in Fig. 6.[14]

In this near anode region, the instability seems to be dominated by the gradients in magnetic field, since the variation of electron temperature and density are, in general, smaller. Because of this reason, we have used only the two field model to study the instabilities in this region. The corresponding growth rates and frequencies are plotted in Fig. 7.

It is clear that the growth rate for profile B_0 is zero, which can be expected since the equilibrium $\mathbf{E} \times \mathbf{B}$ velocity is zero. For the B_{pos} configuration, both the magnetic and density gradient lengths are positive and the growth rate has the values 1.64 MHz, 2.69 MHz, and 3.96 MHz at the axial positions x = 2 mm, 7 mm, and 12 mm from the anode, respectively. For the B_{neg} configuration, the magnetic field and density gradients are both positive and the growth rates at axial positions x = 2 mm, 7 mm, and 12 mm from the anode are 0.99 MHz, 2.0 MHz, and 2.5 MHz, respectively. The frequencies are −4.38 KHz, −13.33 KHz, and −31.92 KHz for B_{pos} at x = 2 mm, 7 mm, and 12 mm and 1.47 KHz, 6.89 KHz, and 11.65 KHz at x = 2 mm, 7 mm, and 12 mm.

C. SPT-100 thruster simulations

To investigate plasma stability, we use plasma parameters in the discharge chamber and the near plume region obtained from simulations of SPT-100 Hall thruster with the HPHall-2 code as reported in Ref. 15. HPHall-2 is a modification[19] of the hybrid fluid/PIC axisymmetric code HPHall[20] that includes more up-to-date wall-sheath and electron mobility models. As reported in Ref. 15, the obtained plasma profiles are in good agreement with the available experimental data for the SPT-100 thruster. Furthermore, the code has been able to reproduce with good agreement the performance parameters of the SPT-100 thruster.[15] The numerically obtained plasma parameters profiles are shown in Fig. 8.

The magnetic field is positive and increasing with distance in the channel region, reaching a maximum at the channel exit and decreasing in the plume region, which results in a positive magnetic field gradient length $L_B = (\partial \ln B/\partial x)^{-1} > 0$ inside the channel and in a negative magnetic field gradient length $L_B = (\partial \ln B/\partial x)^{-1} < 0$ in the plume region. The plasma density reaches its maximum value at a distance of x = 1.5 cm from the anode, decreasing afterwards, resulting in a positive density gradient length $L_N = (\partial \ln n/\partial x)^{-1} > 0$ from x = 0.03 cm to x = 1.5 cm and in a negative density gradient length $L_N = (\partial \ln n/\partial x)^{-1} < 0$ after x = 1.5 cm. We have, then, a region between x = 1.5 cm and x = 2.5 cm where the density and magnetic field gradient lengths are of opposite signs, with the density gradient length being negative and the magnetic field gradient length being positive. This region is

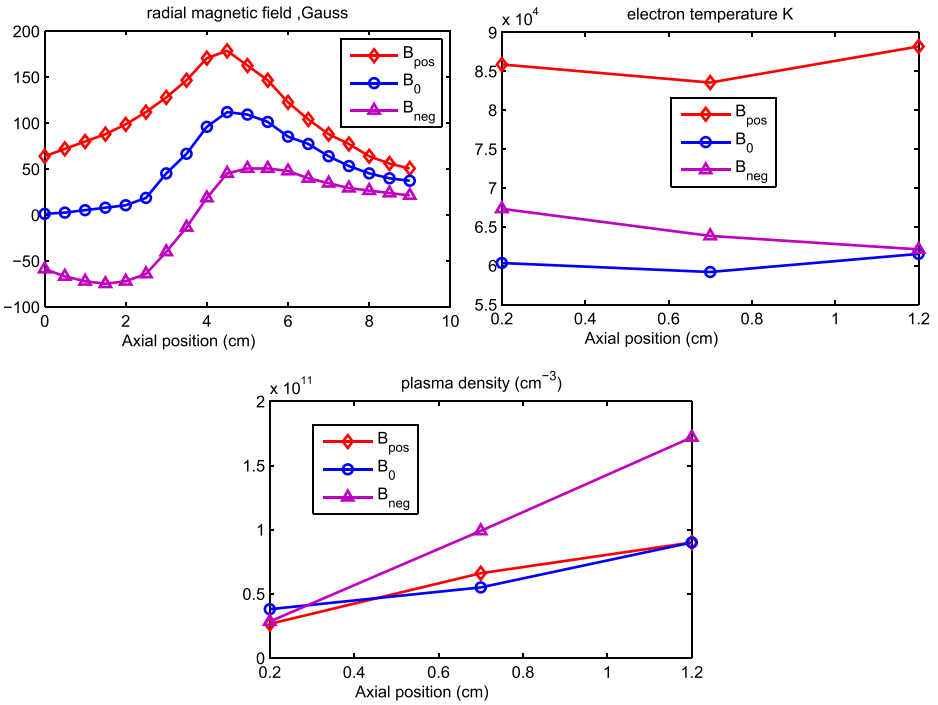

FIG. 6. Three different profiles for magnetic field configuration and electron density and temperature measured at the midpoint between the channel walls as reported in Ref. 14.

expected to be stable. The electron temperature reaches its maximum value also at the exit plane, resulting in a positive temperature gradient length $L_T = (\partial \ln T_e/\partial x)^{-1} > 0$ inside the channel and in a negative temperature gradient length $L_T = (\partial \ln T_e/\partial x)^{-1} < 0$ in the plume. Similarly to the magnetic field and electron temperature, the electric field reaches its maximum value at the exit plane. The gradient lengths for the plasma parameters from Fig. 8 are plotted in Fig. 9.

The growth rate and frequency (of the unstable modes only) calculated by solving Eqs. (4) and (6) are shown in Fig. 10.

For the profiles shown in Fig. 8, there is an unstable region inside the channel from $x = 0.03$ cm to $x = 0.8$ cm, which is close to the anode. This instability growth rate is in the 100–450 KHz range, the growth rate being larger when the temperature gradients are not considered. In this region, $1/L_N - 2/L_B > 0$ and since the electric field and the magnetic field gradient length are both positive, the factor $eE_0/T_e + 2/L_B$ is positive, resulting in instability. The real part of the frequency is determined by the sign of $1/L_N - 2/L_B$. In the unstable region from $x = 0.03$ cm to $x = 0.8$ cm, the frequency is negative due to the factor

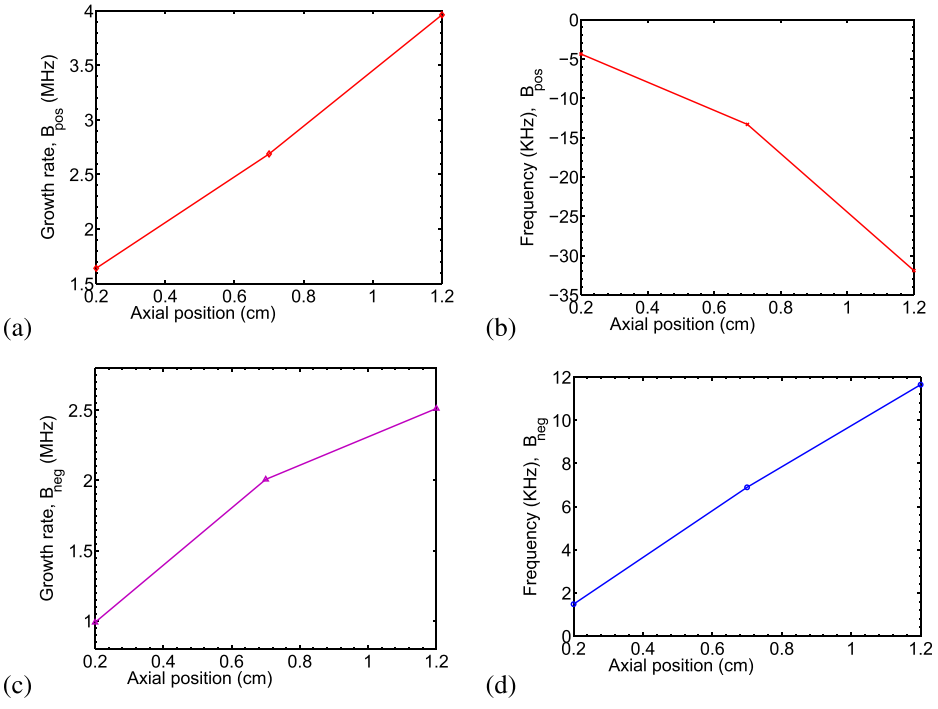

FIG. 7. Growth rate and frequency of the instabilities as a function of axial distance as predicted by the two-field model for the profiles in Fig. 6.

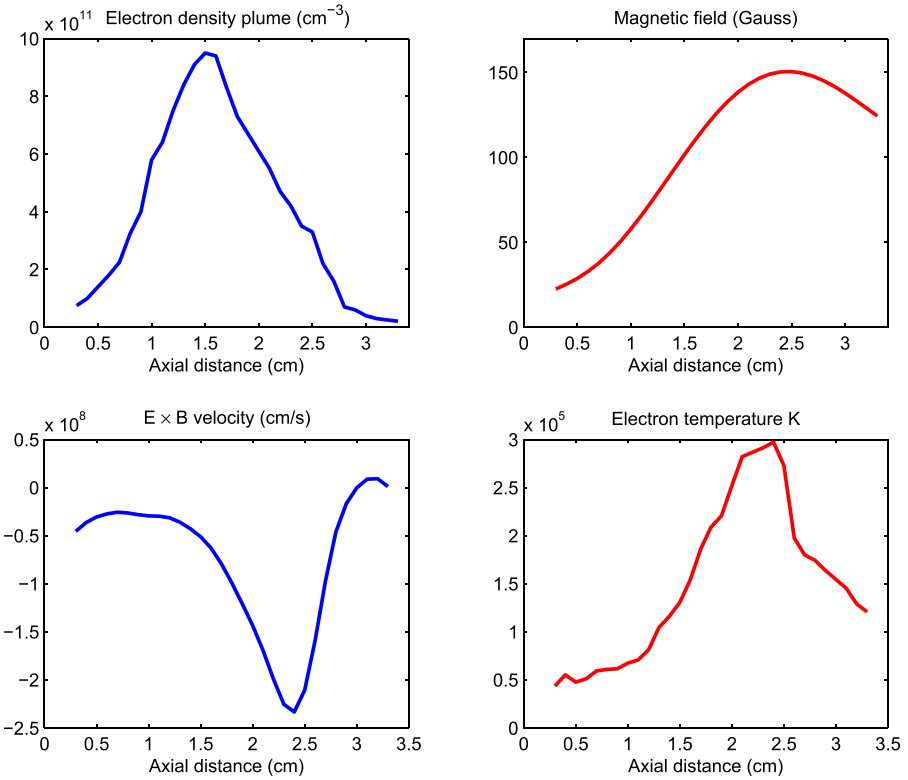

FIG. 8. Plasma density, magnetic field, electron equilibrium drift velocity, u_0, and electron temperature profiles in SPT-100 Hall thruster obtained from HPHall-2 simulations as shown in Fig. 10 from Ref. 15. The exit plane is at x = 2.5 cm.

$1/L_N - 2/L_B$ being positive. For x between 0.8 cm and 2.5 cm (exit plane), the plasma density decreases with distance while the magnetic field is still increasing, resulting in density and magnetic field gradient lengths of opposite signs. In this region, $1/L_N - 2/L_B$ changes sign, becoming positive, while at the same time $eE_0/T_e + 2/L_B$ remains positive, killing the instability. After the magnetic field reaches its maximum value at the exit plane, the magnetic field gradient length becomes negative. From x = 2.5 cm to x = 3.0 cm, we have $1/L_N - 2/L_B < 0$, but the electric field is larger than the threshold value $2T_e/e|L_B|$ resulting in this region being stable.

The growth rate predicted by the three field model is concentrated in the regions from x = 0.03 to x = 0.9 cm and from x = 3.0 to x = 3.2 cm. In the first region, the growth rate predicted by the three field model is considerably smaller than the one predicted by the two field model (maximum values of 450 KHz and 154 KHz), whereas in the

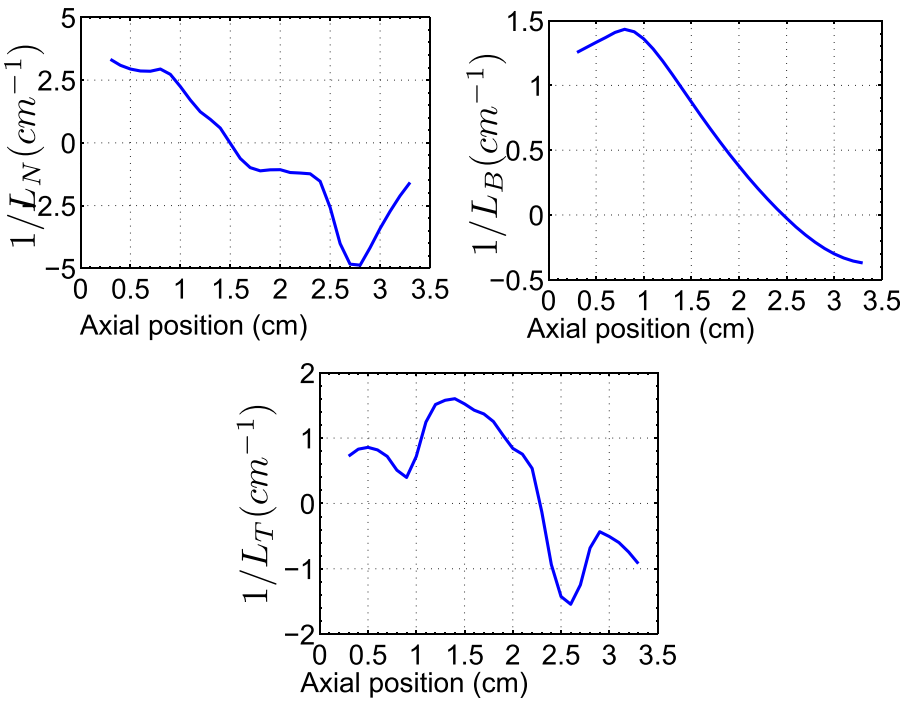

FIG. 9. Gradient lengths for the channel region of SPT-100 Hall thruster. The exit plane is at x = 2.5 cm.

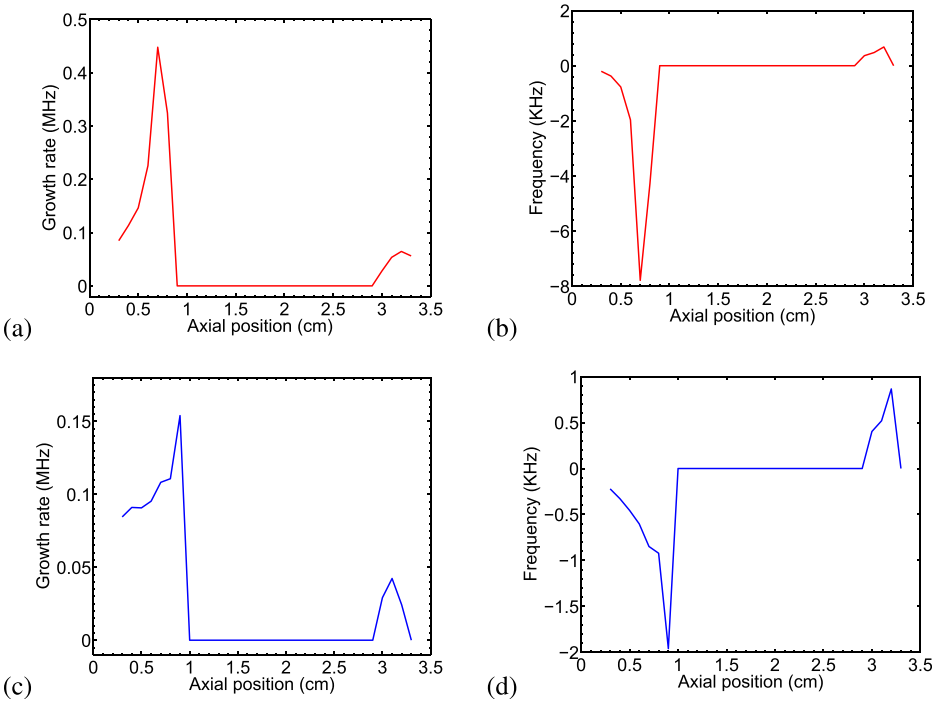

FIG. 10. Growth rate and frequency of the instabilities in a SPT-100 thruster[15] as a function of axial distance to the anode as predicted by the two-field model ((a) and (b)) and the three-field model ((c) and (d)). The exit plane is at x = 2.5 cm.

second region, the growth rate predicted by the two field model is just slightly larger (maximum values of 64 KHz and 43 KHz). The real part of the frequency predicted by the three field model follows the same pattern as the one predicted by the two field model. In the unstable region in the near anode region, from x = 0.03 cm to x = 0.8 cm, the frequency is negative.

There is an interesting feature in the region between x = 3.0 cm and x = 3.2 cm, where the unstable modes propagate with positive frequency. The change of the direction of the rotation is not related to temperature gradients (as was the case in the HTX plume region, see Fig. 3(d)), which is small here and therefore the two and three field model give similar results. In this region, the electric field, within the accuracy of the measurements, is smaller than the threshold electric field, $E < E_{thr}$ (situation unique among all the regions investigated in this paper), and the instability criterion is simply determined by the sign of the factor $1/L_N - 2/L_B$; the mode is unstable for $1/L_N - 2/L_B < 0$. The sign of the real part of the frequency is only determined by the sign of $1/L_N - 2/L_B$, so that the instable modes propagate with positive frequency (in the direction opposite to $\mathbf{E}_0 \times \mathbf{B}_0$). Generally, two field model predicts that the direction of propagation of unstable modes is directly linked to the sign of the quantity $(\mathbf{E}_0 - \mathbf{E}_{thr}) \times \mathbf{B}_0$, thus negative (in the direction of $\mathbf{E}_0 \times \mathbf{B}_0$ flow) for $E_0 > E_{thr}$, and positive when $E_0 < E_{thr}$. Some experiments with $\mathbf{E}_0 \times \mathbf{B}_0$ plasmas do show the presence of fluctuations with rotation in the direction opposite to $\mathbf{E}_0 \times \mathbf{B}_0$ drift.[21] Since our results are very sensitive to the details of plasma parameters profiles, at this time, we cannot confirm that profiles measurements and postprocessing (e.g., profiles gradients) are accurate enough to make conclusive statements regarding the robustness of the rotation against the direction of $\mathbf{E}_0 \times \mathbf{B}_0$ in the experimental conditions discussed in this paper. Indeed, a small perturbation of the plasma plume (induced by the probe, for example) could alter these measurements. More accurate measurements are needed to corroborate the predictions of our model.

D. CAMILA thruster simulations

The CAMILA thruster, developed at the Technion's Asher Space Research Institute, is an effort to adapt Hall thruster technology to low power regimes.[16] In this device, two concentric cylindrical electrodes are used as an anode. The thruster channel consists of the anode cavity and the dielectric walls of the thruster. The magnetic circuit produces a longitudinal magnetic field inside the anode cavity, thus reducing the electron mobility in the radial direction. A radial electric field is created in the direction towards the center of the channel. The radial electric field will increase electron energy in such a way that the gas inside the cavity will be ionized. One advantage of this configuration is that the whole length of the channel can be used for ionization. Two configurations are currently under development, simplified CAMILA, without anode coils and full CAMILA, with anode coils. In the following, we will refer to the simplified version of the thruster. A more detailed description of the CAMILA concept can be found in Ref. 16 and references therein.

The plasma parameter profiles for the CAMILA thruster are shown in Fig. 11 The magnetic field is positive and increasing with distance in the channel region, reaching its maximum value at the channel exit, located at x = 0, which results in a positive magnetic field gradient length $L_B = (\partial \ln B/\partial x)^{-1} > 0$ inside the channel, except for the region from x = −3.0 to − 2.9 cm. The plasma density reaches its

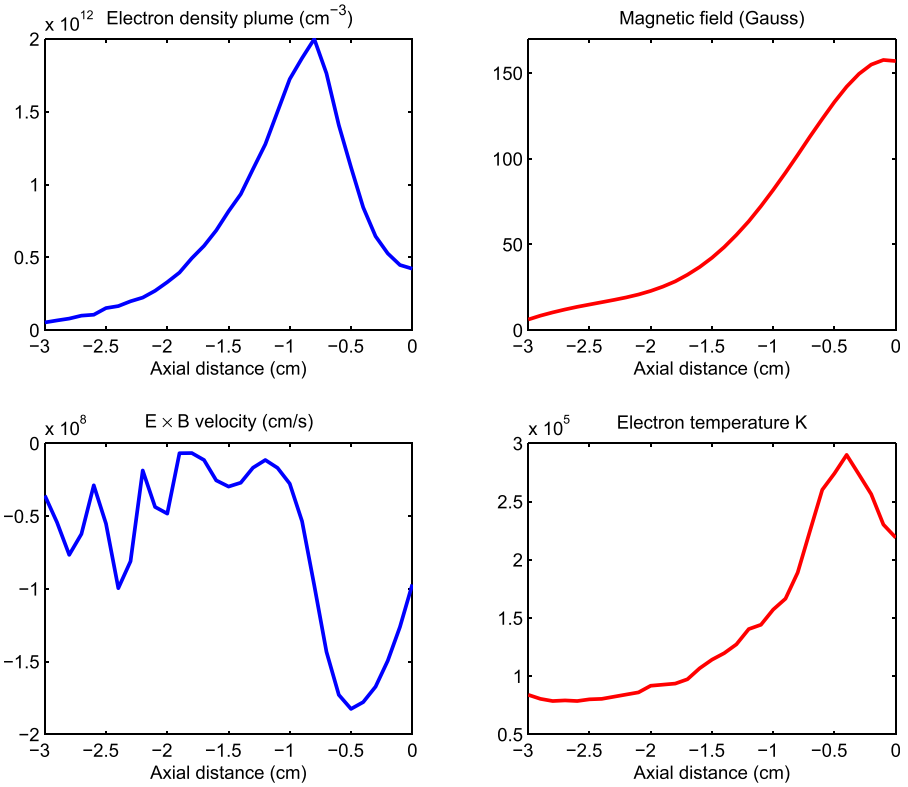

FIG. 11. Plasma density, magnetic field, electron equilibrium drift velocity, u_0, and electron temperature profiles in CAMILA Hall thruster from Ref. 16. The exit plane is at x = 0.

maximum value at a distance of x = −0.8 cm from the exit plane, decreasing afterwards, resulting in a positive density gradient length $L_N = (\partial \ln n/\partial x)^{-1} > 0$ from x = −3.0 cm to x = −0.8 cm and in a negative density gradient length $L_N = (\partial \ln n/\partial x)^{-1} < 0$ from x = −0.8 cm up to the exit plane. We have, then, a region between x = −3.0 and −2.9 and x = −0.8 cm to x = 0 where the density and magnetic field gradient lengths are of opposite signs, with the density gradient length being negative and the magnetic field gradient length being positive. The instability is not present in this region. The electron temperature reaches its maximum value close to the exit plane, at x = −0.4 cm, resulting in a positive temperature gradient length $L_T = (\partial \ln T_e/\partial x)^{-1} > 0$ for most of the region under consideration. Similarly to the magnetic field and electron temperature, the electric field reaches its maximum value at the exit plane. The gradient lengths for the plasma parameters from Fig. 11 are plotted in Fig. 12.

One peculiarity of the CAMILA magnetic field is the additional presence of an axial component. This way, the magnetic field B_0 in dispersion relations, Eqs. (4) and (6), refers to the magnitude of the field. The growth rate and frequencies of the unstable modes calculated by solving Eqs. (4) and (6) are shown in Fig. 13.

For the profiles shown in Fig. 11, there are two unstable regions close to the anode. The first of these regions corresponds to the interval from x = −2.8 cm to x = −2.5 cm, where the maximum value for the growth rate is 280 KHz at x = −2.5 cm. The second unstable region corresponds to the interval from x = −2.0 cm to x = −1.9 cm, where the peak of the growth rate is 367 KHz at a position x = −2.0 cm. These two unstable regions have $1/L_N - 2/L_B > 0$ and since the electric field and the magnetic field gradient length are both positive, the factor $eE_0/T_e + 2/L_B$ is positive, resulting in the appearance of the instability. For x between −1.9 cm and the exit plane, the plasma density decreases with distance while the magnetic field is still increasing, resulting in density and magnetic field gradient lengths of opposite signs. In this region, the factor $1/L_N - 2/L_B$ becomes negative while $eE_0/T_e + 2/L_B$ remains positive, resulting in the disappearance of the instability. In the unstable regions, since $1/L_N - 2/L_B > 0$, the real part of the frequency is negative.

Using the three field model, the instability exists from x = −2.9 cm to x = −2.4 cm and has a maximum value of 508 KHz at x = −2.4 cm and from x = −2.1 cm and −1.7 cm, with a maximum value of 210 KHz at x = −1.7 cm. Similar to the previous examples, the growth rate of the

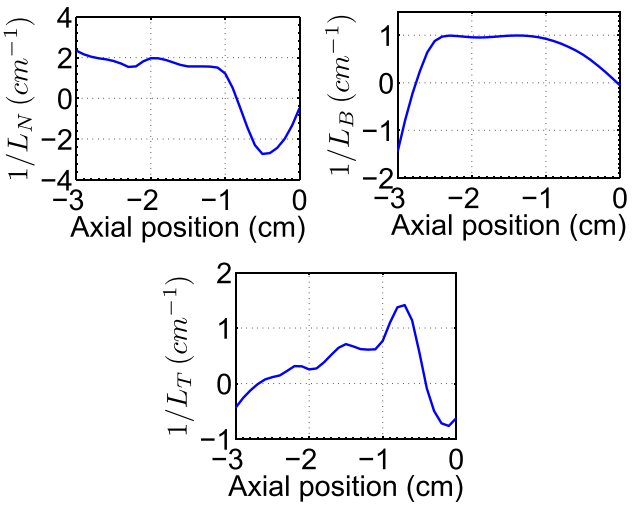

FIG. 12. Gradient lengths for the channel region of CAMILA Hall thruster. The exit plane is at x = 0.

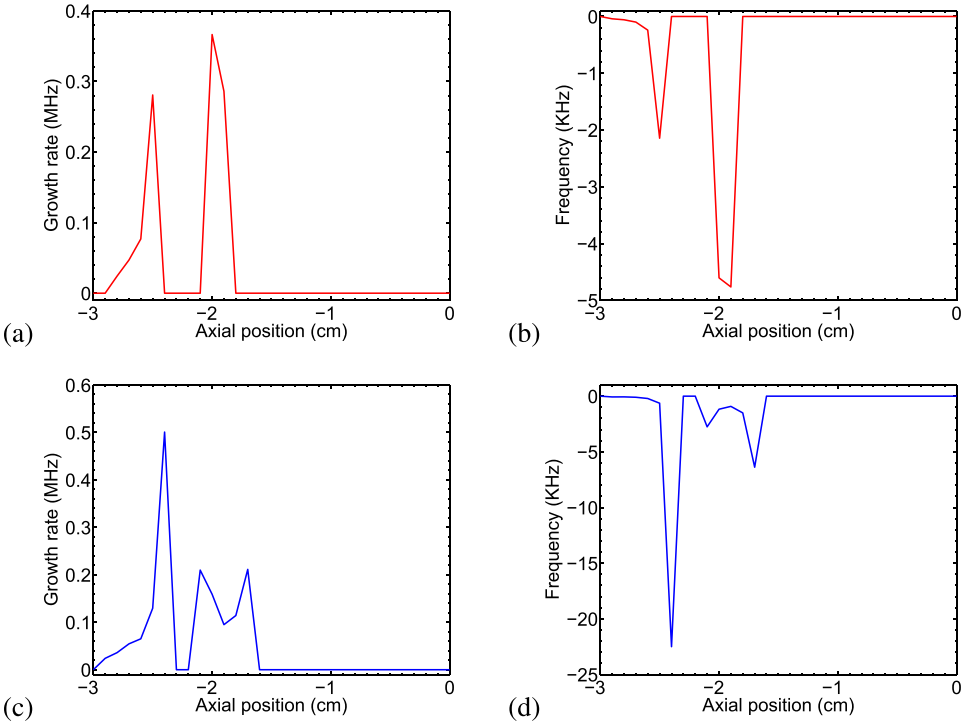

FIG. 13. Growth rate and frequency of the instabilities in the CAMILA thruster[16] as a function of axial distance to the anode as predicted by the two-field model ((a) and (b)) and the three-field model ((c) and (d)). The exit plane is at x = 0.

instability is smaller when the temperature gradients are considered, but in this case, the unstable region is continuous and somewhat broader than that of the two field model. For the three field model, the real part of the frequency is negative.

IV. SUMMARY

The dispersion relations for the two and three field models derived in Part I were used to study the instabilities in four different configuration using the experimental and simulations results. It is interesting that for all configurations, the instabilities are in the near anode and in the plume regions, where the gradient lengths are of the same sign, positive for the near anode region and negative in the plume region. In addition to this, the instability exists in regions between the change of sign of either one of the factors $1/L_N - 2/L_B$ and $eE_0/T_e + 2/L_B$, with sharp peaks in the regions where there is a change of the sign in the factor $1/L_N - 2/L_B$. This condition follows from Eq. (5), where both factors $1/L_N - 2/L_B$ and $eE_0/T_e + 2/L_B$ are required to be of the same sign. One important result is that the Morozov condition predicts instability in a wider spatial region than the one predicted by our model. Also in the plume region, where the magnetic field gradient length is negative, when the factor $1/L_N - 2/L_B$ is positive, the instability requires that the electric field be larger than a certain threshold value given by $E_{0,thr} = 2T_e/e|L_B|$. If the contrary happens, that is, $1/L_N - 2/L_B < 0$, like in the unstable region in the plume of the SPT-100 thruster, the instability occurs if the electric field is smaller than the threshold $E_{0,thr} = 2T_e/e|L_B|$. In the near anode region, since the magnetic field gradient length and the factor $eE_0/T_e + 2/L_B$ (for $E_0 > 0$) are positive, the instability requires that $1/L_N - 2/L_B > 0$.

The highest growth rates are observed in the plume region for the HTX thruster and in the near anode region for the SPT-100 and CAMILA thrusters. In all thrusters, the addition of temperature gradients reduces the peak value of the instability, with the reduction being in as much as 40% for the plume region of the HTX thruster, 60% for the near anode region of the SPT-100 thruster, and 50% for CAMILA. In the near anode region of the HTX thruster, with the magnetic field near the anode, the magnetic field gradient dominates over the density and temperature gradients and the predictions of the two and three field model do not differ considerably.

The conditions for the instability are different depending on the sign of plasma density and magnetic field gradients. Particular conditions existing in different thrusters are summarized in Table I. In the near anode region, where the gradients of the magnetic field and density are both positive, the instability is driven by large density gradient, while the magnetic field gradient is stabilizing. In the plume region, where the gradients of the magnetic field and density are both negative, either magnetic field gradient or the density gradient can be destabilizing, depending on the amplitude of the electric field.

The azimuthal phase velocity of the instabilities, defined as ω_r/k_y, has a maximum value of around $-15\,000$ m/s for

TABLE I. Conditions for instability in different regions of Hall thrusters. Condition I: $\frac{1}{L_N} - \frac{2}{L_B} > 0$, $E > E_{thr}$. Condition II: $\frac{1}{L_N} - \frac{2}{L_B} < 0$, $E < E_{thr}$.

Thruster	Near anode ($L_B, L_N > 0$)	Plume ($L_B, L_N < 0$)
HTX (Ref. 13)	No data	I
HTX (Ref. 14)	I	No data
SPT-100 (Ref. 15)	I	II
CAMILA (Ref. 16)	I	No data

the plume region of HTX, −1500 m/s for the anode region of HTX with the B_{pos} configuration and 600 m/s with the B_{neg} configuration, −40 m/s for both SPT-100 and CAMILA. These values are close to the azimuthal phase velocities observed for the rotating spoke instability.[4]

It is interesting to note that despite difference in designs, all configurations studied here show common feature of the instabilities concentrated in the region near the anode and in the plume region (as far as available data show) and the absence of the instabilities in the acceleration region of the thrusters, close to the maximum values of the electric and magnetic fields.

The primary driving source of the long wavelength instabilities studied in this paper is the equilibrium electron current. The instability can be triggered by collisions, as considered in Ref. 22 or by gradients of plasma density, temperature, and/or magnetic field, which are considered in this paper. Various approximations lead to several different models discussed in the Introduction. Our result for two-fluid model differs in numerical factors from the model by Kapulkin in Ref. 8 because of their incomplete account of compressibility, for more details see Part I. In Fig. 14, the growth rate of the instabilities derived by Kapulkin (Eq. (19) in Ref. 8) is compared with the growth rate predicted by our two-field-model. The growth rate for the anti-drift instability from Eq. (9) is also shown in the same figure. The growth rate predicted by the Kapulkin model is larger than the one predicted by the two-field model in the near anode region, but it is smaller in the plume region. The growth rate is significantly smaller without the gradients of the magnetic field as, as predicted by Eq. (9).

The real part of the frequency for various discharges is shown in Figs. 3, 10, and 13. The mode phase velocity is typically in the same direction as $\mathbf{E}\times\mathbf{B}$ drift (which is negative in our notations) but it is not related to the $\mathbf{E}\times\mathbf{B}$ drift directly. Rather, it is determined by the inverse of the $\omega_* - \omega_D$ frequency (see Eq. (4)). As a result, the real part of the frequency scales inversely with the ion mass, $\omega_r \sim m_i^{-1}$; the growth rate has inverse dependence on the square root of the ion mass, $\gamma \sim (m_i)^{-1/2}$. As follows from our calculations, the phase velocity of this mode is roughly one order of magnitude lower than $\mathbf{E}\times\mathbf{B}$ velocity (for typical parameters considered here), that is consistent with the spoke phase velocity.[4] The inverse mass dependence seems also generally consistent with spoke velocity in other experiments,[23–25] which may suggest that drift gradient modes are responsible for spoke phenomena and no critical ionization phenomena may be involved. As was noted in the Introduction, partial magnetization of ion motion results in the additional term $k_y v_{\theta i}$ to the real part of the frequency. This is the regime of the so called modified Simon-Hoh instability, see Ref. 12 and references therein. Calculation of the average ion drift velocity $v_{\theta i}$, in general, requires knowledge of the global electric field profile and is not attempted here. An estimate based on Eq. (10) predicts[12] that $k_y v_{\theta i}$ contribution may be comparable or exceed the real part of the frequency for the anti-drift mode in Eq. (4), thus changing the scaling for the real part of the mode frequency from $1/m_i$ for the anti-drift mode to $1/\sqrt{m_i}$ for the modified Simon-Hoh mode. It is worth noting that though the near marginal stability boundary effects of magnetic field gradient result in higher values of the real part of the frequency, the role of the ion azimuthal drift may be less pronounced.

As was discussed in the Introduction, Esipchuk and Tilinin have considered physically similar model of the gradient drift instability but used the relations (12) and (13) to express the density gradient via the electric field resulting in Eq. (16). The solution of Eq. (16) is compared with the solution to the two field model dispersion relation (Eq. (4)), for the profiles in Figs. 1, 8, and 11 in Fig. 15. As one can see

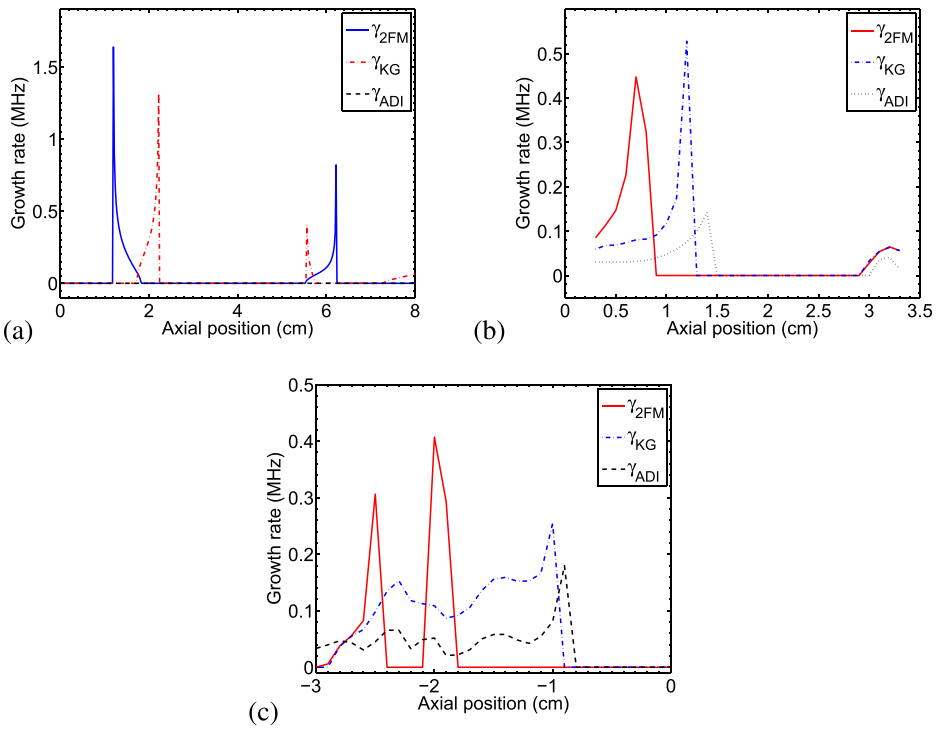

FIG. 14. Growth rate of the instabilities for the (a) HTX thruster, (b) SPT-100, and (c) CAMILA, as predicted by the two-field model, Eq. (19) from Ref. 8 and antidrift instability.[6,12]

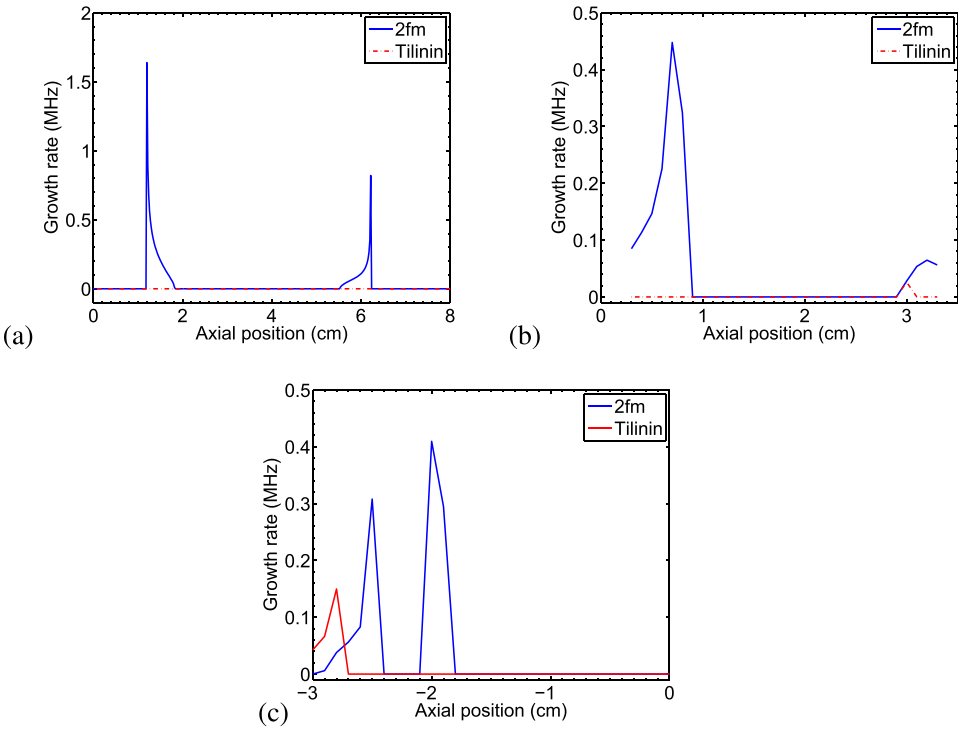

FIG. 15. Growth rate of the instability as predicted by the two field model and by Eq. (16) for (a) HTX thruster, (b) SPT-100, and (c) CAMILA.

from Fig. 15, there is substantial difference between these models: essentially the model of Eq. (16) does not predict the instability in most of the regions. If we would have used the model with the actual density profile, as in Eq. (17), the predictions will be similar to the Kapulkin model, with only quantitative differences with our two-fluid model as shown in Fig. 14.

As was noted above, the derivation of the dispersion relation (16) is based on the assumption that $n_0 v_{0i}$ remains constant. The data confirm that the assumption that $n(x)v_{0i} = \text{constant}$ is not met, especially near the channel exit, as can be seen from Fig. 16. Therefore, the model of Ref. 7, which is typically used in the form given by Eq. (16), gives significantly different results, due to discrepancy of the ion density profile from the $n(x)v_{0i} = \text{constant}$ predictions. The deviation of $n(x)v_{0i}$ from constant may be related to several factors such as radial divergence of the ion flow and ionization processes. In addition to the modification of the equilibrium density profile, ionization process may be lead to specific ionization instabilities,[26] which are not considered here.

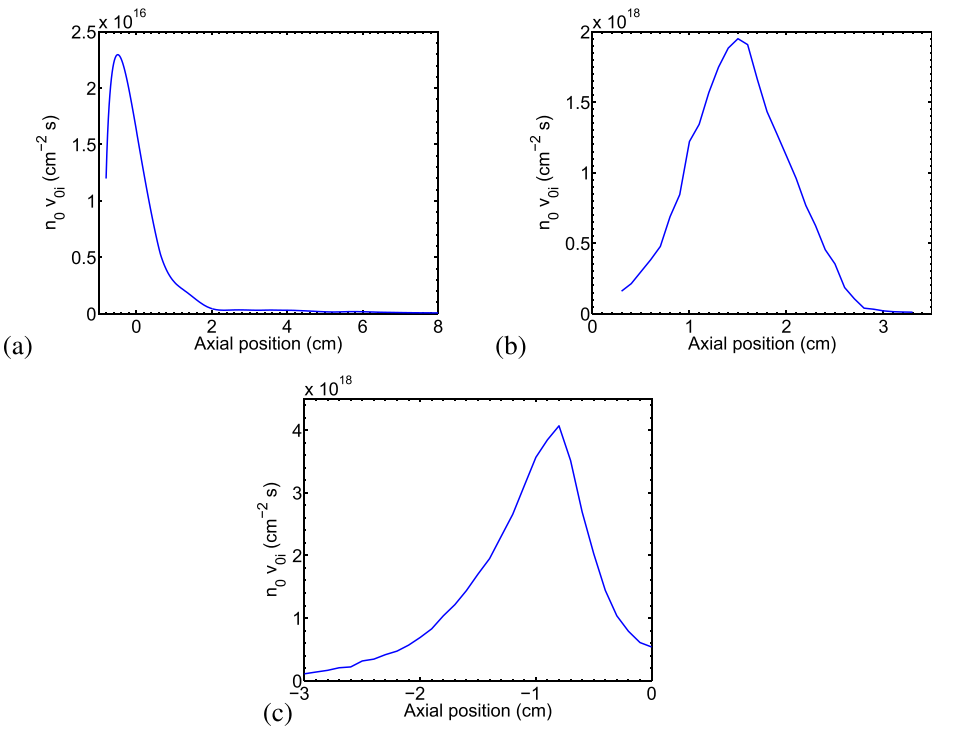

FIG. 16. Product $n_0 v_{0i}$ for the (a) HTX thruster, (b) SPT-100, and (c) CAMILA.

Ducrocq *et al.*[27] also studied the high frequency, short wavelength instability excited by the resonances between the term $k_y u_0$ and harmonics of the electron cyclotron frequency $n\Omega_e$. Such instabilities cannot be described by our fluid theory. According to Ref. 27, for the typical Hall thruster parameters, this instability is robust with respect to the gradients of plasma density and exists mainly in the exit plane of the Hall thruster, where the $E \times B$ drift velocity is maximal. This instability occurs as a result of coupling of the electron cyclotron mode and the ion sound and was studied in detail in Refs. 28–30. These modes are typically highly aperiodic (with growth rates exceeding the real part of the frequency by orders of magnitude), which is consistent with some features observed experimentally.[31] Nonlinear theory and simulations[28–30] predict though that due to large wavevector, these modes saturate at low amplitudes and do not lead to significant anomalous transport.

Our main emphasis was on the analysis of azimuthal modes (with finite k_y). Note that according to Eq. (3), the drift gradient mode may also acquire the axial group velocity due the ion motion in axial direction. Such transit ion modes were studied in Refs. 32 and 33, though the destabilization mechanisms considered in Refs. 32 and 33 were due to collisions and ionization. Our analysis shows that drift gradient effects may also lead to the excitation of the mode with ion group velocity in the axial direction.

The conditions for the linear excitation, general mode characteristics such as frequency and growth rate, the mode localizations of the gradient drift modes studied in this paper are generally consistent with some experimental features, and thus may be responsible for anomalous electron mobility and nonlinear structures. The investigations of the latter require nonlinear theory and nonlinear simulations which are left for other publication.

ACKNOWLEDGMENTS

The authors thank Dr. Nathaniel J. Fisch for helpful discussions, Dr. Richard Hofer for allowing the use of the data from the HPHall-2 simulations and Dr. Igal Kronhaus and Dr. Alexander Kapulkin for providing the data for the CAMILA Hall thruster. This work was sponsored by the Natural Sciences and Engineering Research Council of Canada and partially supported by the Air Force Office of Scientific Research and the US Department of Energy.

[1]M. Keidar and I. Beilis, IEEE Trans. Plasma Sci. **34**, 804 (2006).
[2]G. J. M. Hagelaar, J. Bareilles, L. Garrigues, and J. P. Boeuf, J. Appl. Phys. **93**, 67 (2003).
[3]J. C. Adam, J. P. Boeuf, N. Dubuit, M. Dudeck, L. Garrigues, D. Gresillon, A. Heron, G. J. M. Hagelaar, V. Kulaev, N. Lemoine, S. Mazouffre, J. P. Luna, V. Pisarev, and S. Tsikata, Plasma Phys. Controlled Fusion **50**, 124041 (2008).
[4]C. L. Ellison, Y. Raitses, and N. J. Fisch, Phys. Plasmas **19**, 013503 (2012).
[5]M. E. Griswold, C. L. Ellison, Y. Raitses, and N. J. Fisch, Phys. Plasmas **19**, 053506 (2012).
[6]W. Frias, A. I. Smolyakov, I. D. Kaganovich, and Y. Raitses, Phys. Plasmas **19**, 072112 (2012).
[7]Y. V. Esipchuk and G. N. Tilinin, Sov. Phys. Tech. Phys. **21**, 417 (1976).
[8]A. Kapulkin and M. M. Guelman, IEEE Trans. Plasma Sci. **36**, 2082 (2008).
[9]A. Simon, Phys. Fluids **6**, 382 (1963).
[10]F. C. Hoh, Phys. Fluids **6**, 1184 (1963).
[11]A. M. Fridman, Sov. Phys. Dokl. **9**, 072112 (1964).
[12]Y. Sakawa, C. Joshi, P. K. Kaw, F. F. Chen, and V. K. Jain, Phys. Fluids B **5**, 1681 (1993).
[13]Y. Raitses, D. Staack, M. Keidar, and N. Fisch, Phys. Plasmas **12**, 057104 (2005).
[14]L. Dorf, Y. Raitses, and N. J. Fisch, Phys. Plasmas **13**, 057104 (2006).
[15]R. Hofer, I. Mikellides, I. Katz, and D. Goebel, in 43rd AIAA/ASME/SAE/ASEE Joint Propulsion Conference & Exhibit, AIAA 2007-5267, 2007.
[16]I. Kronhaus, A. Kapulkin, V. Balabanov, M. Rubanovich, M. Guelman, and B. Natan, J. Phys. D: Appl. Phys. **45**, 175203 (2012).
[17]A. Hirose and I. Alexeff, Nucl. Fusion **12**, 315 (1972).
[18]A. I. Morozov, Y. V. Esipchuk, A. Kapulkin, V. Nevrovskii, and V. A. Smirnov, Sov. Phys. Tech. Phys. **17**, 482 (1972).
[19]F. Parra, E. Ahedo, J. Fife, and M. Martinez-Sanchez, J. Appl. Phys. **100**, 023304 (2006).
[20]J. Fife, Ph.D. dissertation, Aeronautics and Astronautics, Massachusetts Institute of Technology, 1998.
[21]T. Ito and M. A. Cappelli, IEEE Trans. Plasma Sci. **36**, 1228 (2008).
[22]A. A. Litvak and N. J. Fisch, Phys. Plasmas **8**, 648 (2001).
[23]N. Brenning and D. Lundin, Phys. Plasmas **19**, 093505 (2012).
[24]A. Lazurenko, L. Albarede, and A. Bouchoule, Phys. Plasmas **13**, 083503 (2006).
[25]A. Lazurenko, G. Coduti, S. Mazouffre, and G. Bonhomme, Phys. Plasmas **15**, 034502 (2008).
[26]D. Escobar and E. Ahedo, in *International Electric Propulsion Conference, Wiesbaden, Germany* (2011), Paper No. IEPC-2011-196.
[27]A. Ducrocq, J. C. Adam, A. Heron, and G. Laval, Phys. Plasmas **13**, 102111 (2006).
[28]C. Lashmore-Davies and T. Martin, Nucl. Fusion **13**, 193 (1973).
[29]M. Lampe, W. M. Manheimer, J. B. McBride, J. H. Orens, R. Shanny, and R. N. Sudan, Phys. Rev. Lett. **26**, 1221 (1971); M. Lampe, W. M. Manheimer, J. B. McBride, J. H. Orens, K. Papadopoulos, R. Shanny, and R. N. Sudan, Phys. Fluids **15**, 662 (1972).
[30]H. V. Wong, Phys. Fluids **13**, 757 (1970).
[31]S. Tsikata, N. Lemoine, V. Pisarev, and D. M. Gresillon, Phys. Plasmas **16**, 033506 (2009).
[32]S. Barral, K. Makowski, Z. Peradzynski, and M. Dudeck, Phys. Plasmas **12**, 073504 (2005).
[33]E. Fernandez, M. K. Scharfe, C. A. Thomas, N. Gascon, and M. A. Cappelli, Phys. Plasmas **15**, 012102 (2008).